Chapter 2

Experimental Techniques and Setup

2.1 Soft X-ray Absorption Spectroscopy

X-ray absorption is a core-level excitation through a transition from a core state to an unoccupied state by absorbing photons. Because every element has characteristic core-level binding energies, x-ray absorption is element specific like all other core level spectroscopies.

2.1.1 Electron-Photon Interaction in XAS

The basic principle governing the x-ray absorption is the interaction of electromagnetic radiation with matter. The interaction can be simplified to a system with one photon interacting with an n-electron atom. The system's Hamiltonian can be expressed as

$$H = H_{atom} + H_{rad} + H_{inter}, \tag{2.1}$$

where H_{atom}, H_{rad}, and H_{inter} are the Hamiltonian of the atom, photon, and their interaction, respectively.

The radiation field is

$$H_{rad} = \hbar\omega(\mathbf{a}^{\dagger}\mathbf{a} + 1/2), \tag{2.2}$$

where $\mathbf{a}^{\dagger}$ is the creation operator and $\mathbf{a}$ is the destruction operator. In non-relativistic approximation, the interacting Hamiltonian is

$$H_{inter} = -\frac{e}{mc}\mathbf{p}\cdot\mathbf{A}, \tag{2.3}$$

where the vector operator of the radiation field can be written as

$$\mathbf{A} = (\frac{2\pi\hbar c^2 n}{V\omega})^{1/2}\hat{e}e^{ikr-wt}, \tag{2.4}$$

and the photon energy is $\hbar\omega$. The transition probability between the initial and final states is

$$M = \langle\Phi_f|H_{inter}|\Phi_i\rangle, \tag{2.5}$$

and the transition rate is given by Fermi's golden Rule:

$$W = \frac{2\pi}{\hbar}|M_{ij}|^2\delta(\hbar\omega - E_f + E_i), \tag{2.6}$$

where $M_{ij} = \langle 2p^5 3d^{n+1}|\frac{e}{2m}\mathbf{A}\cdot\frac{\hbar}{i}\nabla|3d^n\rangle$ for a system of n electrons in the $3d$ orbitals.

In an x-ray absorption process, the Fermi's golden rule determines the absorption cross-section, and the matrix element must be non-zero based on the selection rules. The matrix element is also related to the initial and final state of the XAS process.

2.1.2 Ground State

In order to understand the absorption process, it is necessary to know the ground state of the material. In an XAS process, there are two models used to analyze the absorption spectra. One can either use the density functional theory (DFT) or the configuration-interaction scheme to describe the electronic structure of transition metals.

The single-particle description of XAS process works well for the metal and oxygen K-edge in transition-metal oxides. However for the metal $L_{2,3}$-edges absorption, this agreement is rather poor because of the strong wave function overlap of the core and valence states. For example, in NiO, the final state of L-edge x-ray absorption process is a partially filled core state with a $2p^5$ configuration and the final state also has an incompletely filled $3d$ band with a $3d^9$ configuration. The $2p$-hole and $3d$-hole have a wave functions overlaping, which is an atomic effect leading to the so-called multiplet effects. The multiplet effect describes the interaction between the core holes and the partially filled valence band. In contrast, in the case of s-core holes, multiplet effects are reduced [1] to just the exchange interaction between the spin of the s-core hole and valence electrons, and the exchange interaction is small, implying that multiplet effects will not be visible.

In short, the $s \rightarrow p$ absorption can be approximately described with density functional theory. In the $p \rightarrow d$ transition, the single-particle picture breaks down and the multiplet effect dominates.

Density Functional Theory

In 1930's, physicists were aware of the quantum mechanical equations to solve the many-electron systems, but were incapable of solving the systems exactly except some simple cases. In 1964, Walter Kohn and Pierre Hohenberg proved the density functional theory [2] for understanding many-electron systems. In place of the complicated functions which depend on the position of each electron in the system, they showed that knowing the average density of electrons at all points in space was enough to uniquely determine the total energy and all other physical properties of the system. Furthermore, this ground-state electron density can be found by solving a self-consistently one-electron Schrödinger equation. In 1965, the density functional theory was greatly enhanced after W. Kohn and L. J. Sham described a procedure for driving the electron density of ground state and total energy of a system [3], the so-called local density approximation (LDA). The trick was to separate the universal function into three parts: kinetic energy, Coulomb energy, exchange and correlation energy.

The DFT theory help us understand the band structure of a system. The occupied and unoccupied states are equally important for understanding the physical properties involving low-energy excitations from the states below Fermi level and to those above. This is not only to determine the total energy but also to obtain a picture of the electronic structure, which is used to analyse the XAS spectra. Figure 2.1 shows one example of comparison of

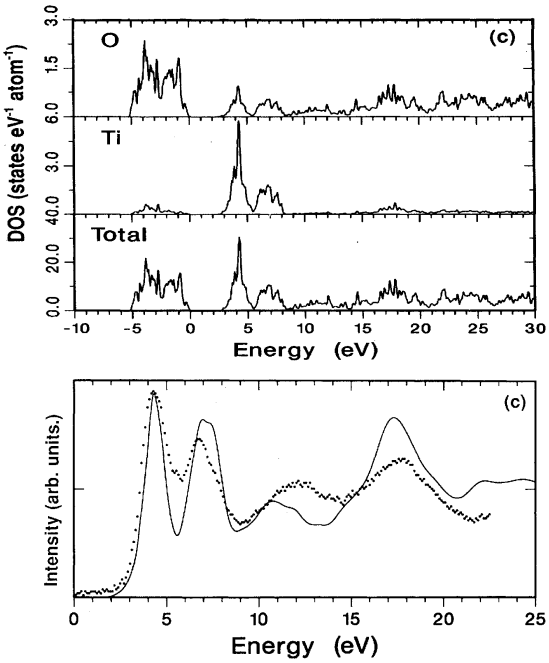

Figure 2.1: **Upper panel**: Site-projected and total density of states of anatase TiO_2. **Lower panel**: The oxygen $1s$ XAS (dotted line) and the oxygen p-projected density of state. (solid line) of TiO_2 (from Ref. [4]).

the oxygen K-edge XAS spectra with the oxygen projected density of states for anatase TiO_2 [4].

Multiplet Effects

Atomic multiplet describes the L-edge XAS process between the configuration of the initial and final states including the Hund's rule. The allowed transitions depend on the selection rules, and the transition rate is determined by Fermi's golden rule.

The L-edge absorption process in transition metals is a transition process of $3d^n$ initial state to $2p^5 3d^{n+1}$ final state by means of a dipole transition. The dominant transitions are $2p_{1/2} \longrightarrow 3d$ (denoted as L_3-edge) and $2p_{3/2} \longrightarrow 3d$

(denoted as L_2-edge), with an energy separation determined by the spin-orbital coupling. In $3d$ transition-metal oxides, one-electron model is not a good approximation for L-edge XAS.

Ligand-Field Multiplet Theory

In the case of the $3d$-metal oxides, one has to include the hybridization between the oxygen $2p$-band and transition-metal $3d$-band to describe the XAS spectra correctly. The transition-metal ions are surrounded with oxygen ligand; it is necessary to include the symmetry effect of the oxygen neighbors. The local symmetry can be described in terms of ligand-field multiplet theory (or so-called crystal field multiplet theory).

A large range of transition-metal oxides systems consist of a metal ion surrounded by six neighboring oxygen atoms and form a so-called octahedral structure, dominantly in cubic solids. In the octahedral environment, the field of the neighboring atoms on the central atom has the cubic (O_h) symmetry which divides the 5-fold degenerate $3d$-orbitals into two symmetries, t_{2g} and e_g. The 2-fold degenerate e_g state contains orbitals which is directly toward the position of ligand, so e_g states interact stronger with the ligand. The three t_{2g} orbitals point toward the corners of the cubic; therefore, their interaction with the octahedral ligands is smaller. The strength of dominant symmetry effect is the ligand-field splitting ($10D_q$).

The effect of the cubic ligand field on the energies of the atomic states has been described in the textbooks [5, 6, 7]. For example, the $3d^0$ configuration

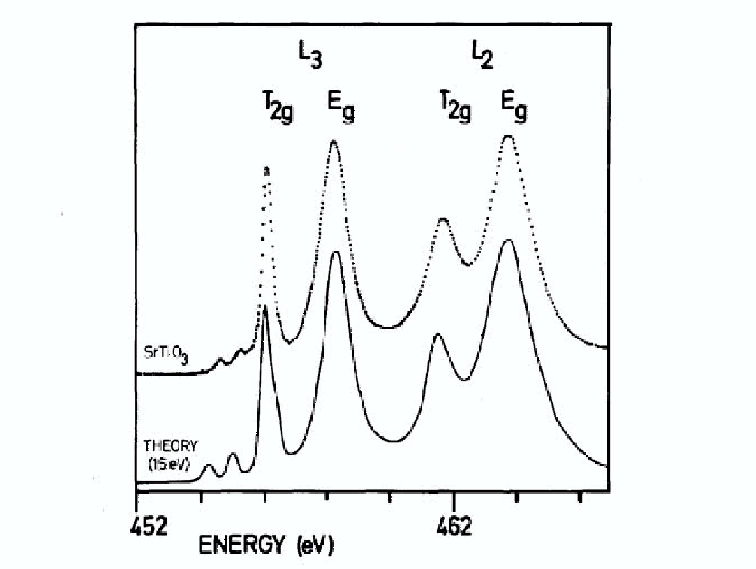

Figure 2.2: Multiplet spectrum for $3d^0 \rightarrow 2p^5 3d^1$ of Ti^{4+} with crystal field. The solid line shows that crystal field $10D_q$ was taken as 1.5eV, and the dashed line is the $SrTiO_3$ $2p$ x-ray absorption spectrum (from Ref. [8]).

of Ti^{4+} in cubic symmetry, all final states with T_1 symmetry are allowed transition from the A_1 initial state. In Fig. 2.2 [8], solid line shows the effects of ligand field on multiplet spectrum with the $10D_q$= 1.5eV, and dashed line displays the $SrTiO_3$ L-edge x-ray absorption spectrum. The calculation reproduces all peaks which are visible in experiment, especially well observed in the small pre-peaks.

Change-Transfer Multiplet Theory

Because of the configuration-interaction effect, charge fluctuations allow more than one electronic configurations in the initial and final states.

In transition-metal oxides, when an electron of oxygen valence $2p$-band fluctuates to the metal $3d$-band, the configuration of initial state can be

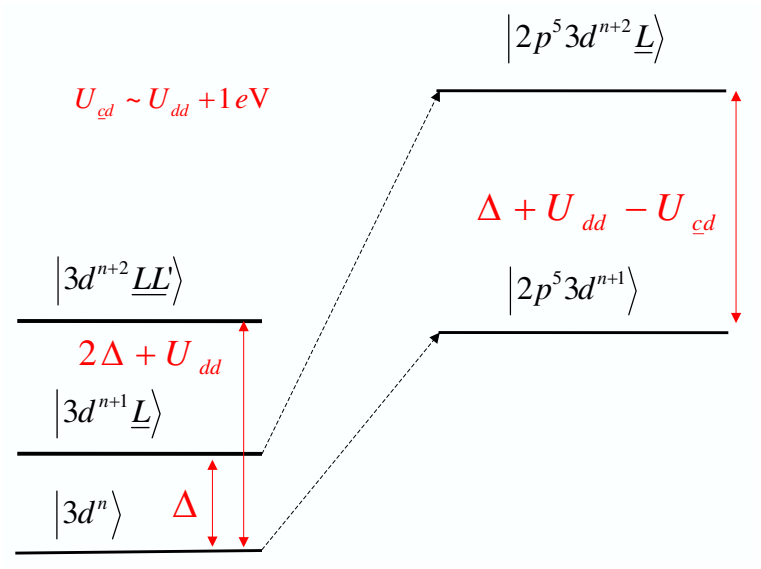

Figure 2.3: X-ray absorption process described with charge transfer. All the notations are explained in the text.

expressed as $3d^{n+1}\underline{L}$ (the $\underline{L}$ denoting a ligand hole in oxygen). The charge transfer model adds a configuration $3d^{n+1}\underline{L}$ to the $3d^n$ ground state. The energy difference between the $3d^n$ and $3d^{n+1}\underline{L}$ configuration is the charge transfer energy, as described in Chapter 1. A higher order configuration $3d^{n+2}\underline{L}\,\underline{L}'$ can also exist in the initial state. In many cases, charge-fluctuation configurations are reguired to explain the spectral shapes.

As shown in Figure 2.3, if the $3d^{n+2}\underline{L}\,\underline{L}'$ including, the energy difference between the $3d^{n+2}\underline{L}\,\underline{L}'$ and $3d^n$ is $2\triangle + U_{dd}$. The U_{dd} is the on-site Coulomb energy of $3d$-electrons, defined as the required energy to transfer a d-electron from a metal site to another, i.e., $3d^n + 3d^n \rightarrow 3d^{n+1} + 3d^{n-1}$.

In the final state of an XAS process, the configurations are $2p^5 3d^{n+1}$ and $2p^5 3d^{n+2}\underline{L}$. The energy difference between $2p^5 3d^{n+1}$ and $2p^5 3d^{n+2}\underline{L}$ is

$\triangle + U_{dd} - U_{\underline{c}d}$, where $U_{\underline{c}d}$ is the core hole potential (which will be discussed in next section). Empirically $U_{\underline{c}d}$ is slightly 1 eV larger than U_{dd} for transition-metal oxides, i.e. $U_{\underline{c}d} \sim U_{dd} + 1\ eV$ [9].

2.1.3 Final State

The final state of x-ray absorption includes an additional electron excited by the photoelectric process in the valence band and a core hole left behind. The effect of core-valence interaction is important in the final state of XAS.

In the left of Fig. 2.4, without the core-valence interaction, the energy difference between $2p^5 3d^{n+1}$ and $2p^5 3d^{n+2}$ for the final states excited from $3d^n$ and $3d^{n+1}$ ground states, respectively, is the on-site Coulomb interaction energy U_{dd}. However, if the core-valence interaction is included, when a $2p$ electron is excited to the $3d$ band and the final state has $(n+1)$ d-electrons with the $2p^5 3d^{n+1}$ configuration, the final-state energy is reduced by $(n+1)$ times of the core-valence interaction, i.e., $(n+1)U_{\underline{c}d}$. As shown in the right of Fig. 2.4, the energy difference between $2p^5 3d^{n+1}$ and $2p^5 3d^{n+2}$ with core-valence interaction is $U_{dd} - U_{cd}$. The absorption energy of a $3d^n$ configuration in the ground state shifts to the lower-energy side of the absorption spectra by $U_{dd} - U_{\underline{c}d}$, as compared with the absorption of a $3d^{n+1}$ configuration. We therefore can use this energy separation to identify the absorption resulting from different valencies of transition-metal ions.

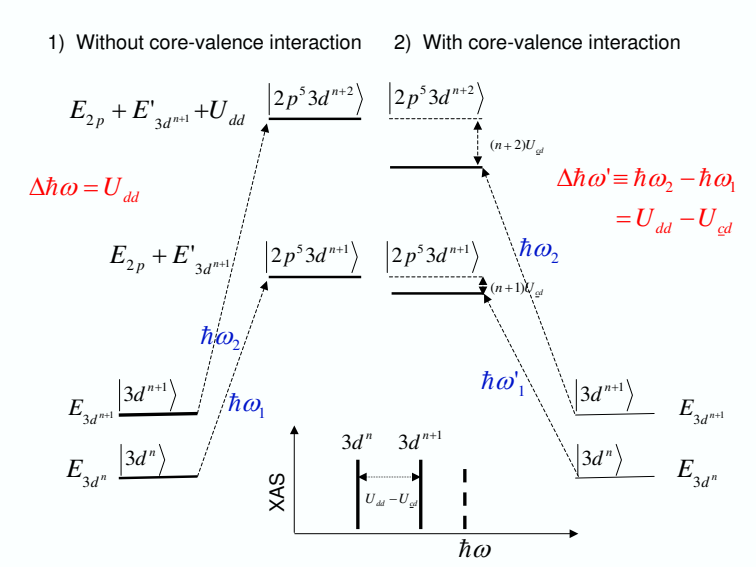

Figure 2.4: The energy diagrams of L-edge x-ray absorption in a compound without and with core-valence interaction.

2.1.4 Matrix Element

X-ray absorption is typically interpreted as a one-electron addition process combined with the core-valence interaction. A core-electron is excited to the unoccupied state, and the transition matrix element M_{ij} determines the absorption cross section. In dipole approximation, the matrix element M_{ij} is non-zero only when the angular quantum number difference between final state and initial state is ± 1 ($\triangle l = \pm 1$, i.e., $s \rightarrow p$ or $p \rightarrow d$, etc.) and the spin quantum number is conserved ($\triangle s = 0$). The quardrupole transition is with $\triangle l = \pm 2$, i.e., $s \rightarrow d$ or $p \rightarrow f$, etc. The quardrupole transition is much weaker than the dipole transition by several orders of magnitude.

Table 2.1 shows the term symbols of $3d^n$-systems and the number of allowed transitions of $3d^n \rightarrow 2p^5 3d^{n+1}$ with the dipole selection rules. For a

Table 2.1: Electronic configuration involving in the transition of L-edge x-ray absorption from the atomic ground state to allowed final state symmetries and after applying the dipole selection rule.

transition	# of term symbols ground state	symmetry of ground state	# of term symbols final state	# of allowed transitions
$3d^0 \rightarrow 2p^5 3d^1$	1	$^1S_0$	12	3
$3d^1 \rightarrow 2p^5 3d^2$	2	$^2D_{3/2}$	45	29
$3d^2 \rightarrow 2p^5 3d^3$	9	$^3F_2$	110	68
$3d^3 \rightarrow 2p^5 3d^4$	19	$^4F_{3/2}$	180	95
$3d^4 \rightarrow 2p^5 3d^5$	34	$^5D_0$	205	32
$3d^5 \rightarrow 2p^5 3d^6$	37	$^6S_{5/2}$	180	110
$3d^6 \rightarrow 2p^5 3d^7$	34	$^5D_2$	110	68
$3d^7 \rightarrow 2p^5 3d^8$	19	$^4F_{9/2}$	45	16
$3d^8 \rightarrow 2p^5 3d^9$	9	$^3F_4$	12	4
$3d^9 \rightarrow 2p^5 3d^1 0$	2	$^2D_{5/2}$	2	1

$3d^3 \rightarrow 2p^5 3d^4$ transition, for example, the term symbol of $3d^3$ ground state in Hund's rules is $^4F_{3/2}$ with $J = 3/2$. The number of term symbols in $2p^5 3d^4$ final state is 180. For dipole selections, only the final states with $J' = 1/2$, $J' = 3/2$ and $J' = 5/2$ are allowed, and the numbers of transition are 21, 35 and 39. This implies a total of 95 allowed peaks out of the 180 final-state term symbols.

In x-ray absorption, the spectral shape reflects the partial density of unoccupied states. However, the absorption spectrum is convoluted with a Lorentzian broadening to account for the finite lifetime of the core-hole following with the Heisenberg's uncertainty principle.

The term symbol only describes the symmetry aspects, but does not depict the relative energy of each multiplet in XAS. The relative strengths

of different terms are determined by the matrix elements with including electron-electron interaction and spin-orbit coupling. The electron-electron interaction can be described as:

$$\langle {}^{2S+1}L_J|\frac{e^2}{r_{12}}|{}^{2S+1}L_J\rangle = \sum_k f_k F^k + \sum_k g_k G^k, \tag{2.7}$$

where the F^k and G^k are the Slater-Condon parameters [10, 11, 12]. F^k and f_k are the radial and angular part of the direct Coulomb repulsion, respectively. G^k and g_k are the radial and angular part of the Coulomb exchange interaction, respectively.

The f_k and g_k are non-zero in certain values of k depending on the term configuration. The direct Coulomb repulsion f_k is present until k equals two times the lowest value of the orbital quantum number l, and the Coulomb exchange interaction g_k is present only for electrons in different shell. For example, it contains non-zero Slater-Condon parameters of f_0, f_2, and f_4 in $3d^n$ configuration. For a $2p^5 3d^{n+1}$ configuration in the XAS final state, the Slater-Condon parameters of f_0, f_2, f_4, g_1, and g_3 are non-zero. The radial part of Slater-Condon parameters F^k and G^k were tabulated in the standard textbook of quantum mechanics [13]. For the $3d$-electron system, the F^2 is approximately equal to 10 eV, and $F^4 = 0.62F^2$.

2.1.5 Linear Dichroism in X-ray Absorption

In x-ray absorption, the matrix element of a dipole transition is proportional to the Gaunt coefficient $c^k(l_1 m_1, l_2 m_2)$ with $k = 1$, where l_1 and m_1

are, respectively, the orbital and magnetic quantum number of one-electron valence orbit, and l_2 and m_2 are those of the core state.

In the dipole transition, $m_1 - m_2$ must be equal to ± 1 for the electric field of the incident x-ray **E** perpendicular ($\perp$) to the z-axis. For the electric field **E** is parallel ($\parallel$) to the z-axis, then $m_1 = m_2$. We can select the transition between m_1 and m_2 by changing the direction of **E** to determine the orbital polarization directly.

If the occupied $3d$-electron cloud has an out-of-plane shape of unoccupied states, the integrated XAS intensity with x-ray $\mathbf{E} \parallel z$ is larger than that with $\mathbf{E} \perp z$. On the other hand, if the electron cloud has an in-plane shape of unoccupied states, the intensity of $\mathbf{E} \perp z$ is larger than that of $\mathbf{E} \parallel z$. The polarization-dependent soft x-ray absorption, particularly linear dichroism, provides us with a powerful tool to identify the orbital polarization of transition-metal oxides.

2.1.6 Examples of XAS

A. Oxygen $1s$ XAS in Transition-Metal Oxides

The oxygen K-edge XAS is the transition which a core-level electron is excited to an unoccupied $2p$-state, i.e. $1s \rightarrow 2p$ transition. The absorption-threshold energy is about 530 eV.

Figure 2.5 shows the oxygen K-edge XAS spectrum of $LaSrMnO_4$ single crystal. The spectrum can be divided into two regions. The first region, near the 530 eV photon energy, is attributed to oxygen $2p$ predominantly hy-

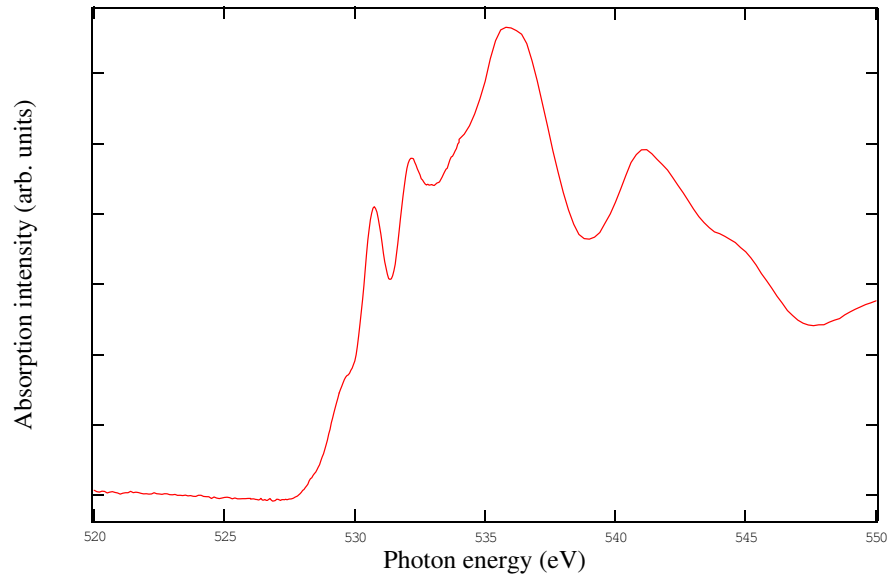

Figure 2.5: Oxygen K-edge x-ray absorption spectrum of $LaSrMnO_4$. The pre-edge peak near 530 eV is assigned to oxygen p character in the transition metal $3d$ band. The broader structure above 540 eV is the oxygen p character hybridized with metal $4s$- and $4p$-bands.

bridizing with transition-metal $3d$-band. The second region, typically 5∼10 eV above the absorption threshold, is attributed to oxygen p character hybridizing with metal $4s$- and $4p$-states.

At the pre-edge XAS, which is related to $3d$ bands, the spectrum consists of two peaks. These two peaks can be identified as the t_{2g} and e_g symmetry separated by ligand-field. To check the validity of these peaks as being related to the t_{2g} and e_g symmetry, we will discuss this question in next chanter.

The oxygen $1s$ XAS in transition-metal oxides also provide us the spectral fingerprint of strong electron correlations. Figure 2.6 shows the example of spectral weight transfer in $La_{2-x}Sr_xCuO_4$ [14], the configuration of Cu is d^9 in the La_2CuO_4. The hole concentration was increasing with the Sr doping x. Two distinct peaks are observed at photon energies around 528.8eV

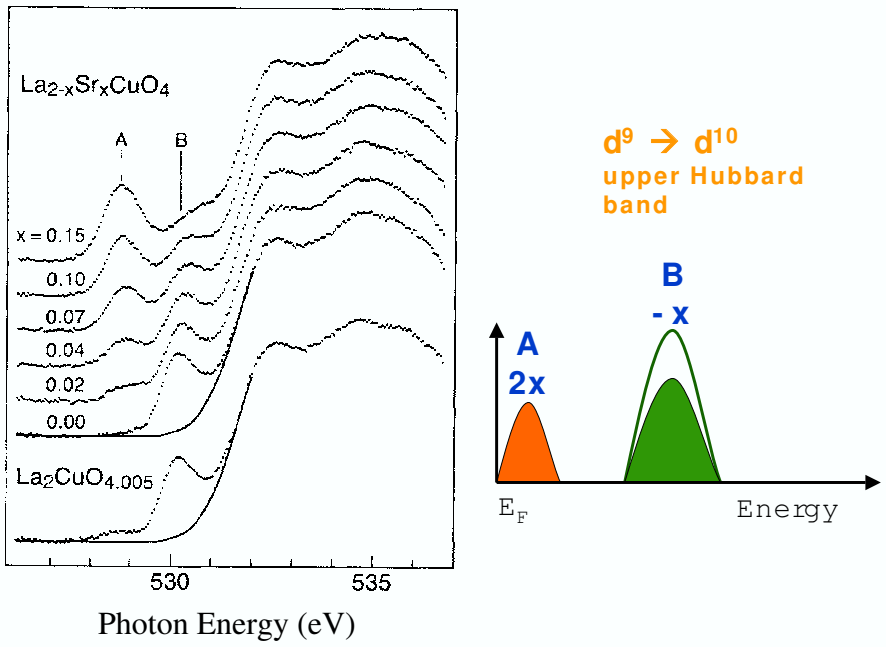

Figure 2.6: Fluorescence yield of oxygen $1s$ x-ray absorption spectrum of the $La_{2-x}Sr_xCuO_4$ with various doping. (from Ref. [14])

(labeled A) and 530.3eV (labeled B). In the O $1s$ XAS, because O $2p$ is strongly hybridized with Cu $3d$-band, oxygen $1s$ XAS spectra also represent the electronic structure of Cu. Peak-B represents the absorption of $3d^9 \rightarrow 3d^{10}$, and peak-A shows that of $3d^9\underline{L} \rightarrow 3d^9$. The peak-B is related to the upper Hubbard band which can be well represented by the one-band Hubbard model. As the doping concentration increases, peak-B decreases but peak-A increases. The ratio between the decrease of peak-B and the increase of the peak-A is 1:2. One spin channel in unoccupied states is involved in the absorption transition of the d^9-configuration. However, in the $d^9\underline{L}$ configuration, both up-spin and down-spin channels contribute to the absorption; the increases of peak-A with hole concentration is two times

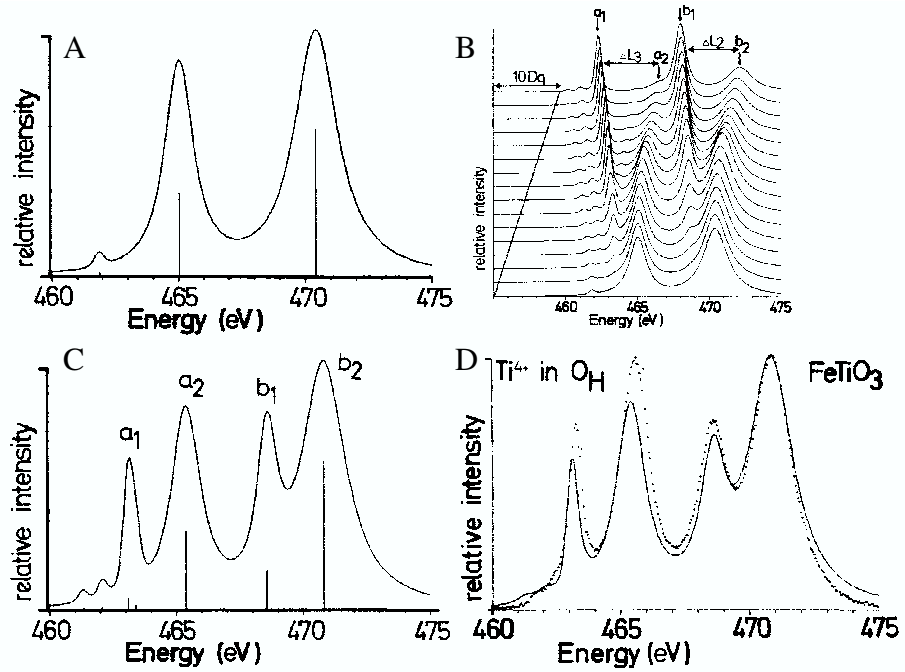

Figure 2.7: (A) Calculated atomic multiplet spectrum of $3d^0 \rightarrow 2p^5 3d^1$ in Ti^{4+}. (B) Atomic multiplet calculation of Ti^{4+} in octahedral symmetry in various $10Dq$ parameters. (C) Multiplet spectrum of Ti^{4+} in $3d^0 \rightarrow 2p^5 3d^1$ excitation with crystal-field $10Dq$ = 1.8 eV. (D) The experiment $FeTiO_3$ XAS spectrum (dotted) is compared with multiplet calculation of (C) in O_h symmetry. (from Ref. [8])

of that of the peak-B. This spectral weight transfer provides us a fingerprint of strong electron correlations.

B. L-edge Absorption in Transition Metal

To illustrate the L-edge absorption of transition metal, multiplet theory including with ligand-field and charge-transfer is needed. Figure 2.7(A) [8] displays the atomic multiplet calculated spectrum for the $3d^0 \rightarrow 2p^5 3d^1$ excitation of Ti^{4+}. Figure 2.7(B) shows the ligand-field multiplet calculations with cubic crystal-field value $10D_q$ from 0.0 eV (bottom) to 4.5 eV (top), and especially the $10D_q = 1.8$ eV was shown in figure 2.7(C). Figure 2.7(D) is the

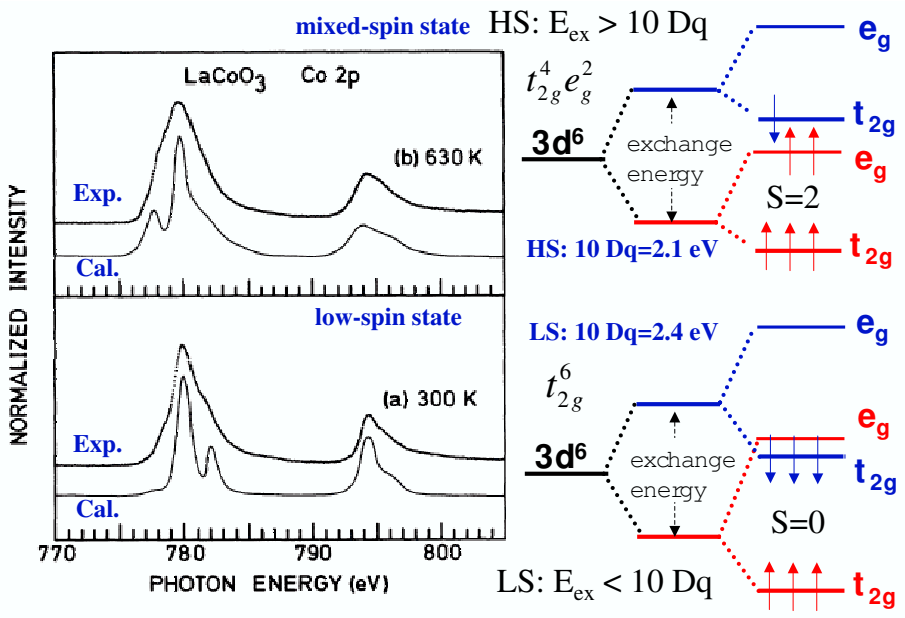

Figure 2.8: Left panel: The experimental Co L-edge XAS spectra of $LaCoO_3$ compared with multiplet simulation. At 300 K, the calculation ia assuming a low-spin state of t_{2g}^6 configuration, as shown in lower right panel. At 630 K, the simulation is assumed in mixed-spin state which is mixed two contributions of the low-spin state (described above) and a high-spin state of $t_{2g}^4 e_g^2$. (from Ref. [15])

experiment $FeTiO_3$ spectrum (dotted), which is compared with ligand-field multiplet calculated result. So, the combination of L-edge XAS technique and multiplet calculation could provide us much information in studying transition-metal oxides.

L-edge x-ray absorption spectroscopy also could provide the information about spin state in transition-metal oxides. Figure 2.8 displays the spin state studies of L-edge XAS in $LaCoO_3$ [15]. The dotted lines shows the Co L-edge XAS spectra of $LaCoO_3$ at 300 K and 630 K. And solid lines are the atomic multiplet simulations. When the $LaCoO_3$ at room temperature (300 K), the simulation shows that the Co^{3+} ion is in low-spin state with $10D_q = 2.4$ eV.

The ground state in room temperature is given by t_{2g}^6 configuration, as shown in the lower-right panel of Fig. 2.8. In addition, the results indicated a transition to a mixed-spin state at high temperatures (630 K). The ground state is including two mixed-spin contributions: the low-spin state described above and a high-spin state of $t_{2g}^4 e_g^2$ configuration with $10D_q = 2.1$ eV. Comparing the XAS results and simulations, we could determine the spin states in transition-metal oxides.

2.2 Experimental Setup of XAS

Modern x-ray absorption studies are made with the use of synchrotron radiation. The most accurate method to measure x-ray absorption spectrum is the transmission mode with recording the intensities of the transmitted and the incident beams. However, the transmission mode requires samples with a thickness smaller than the penetration depth of photons. For many cases, such as transition-metal oxide, the transmission mode is not suitable. Alternatively, we collected the sample drain current, i.e., the total electron yield method, to probe the absorption process of transition-metal oxides. The probing depth of total electron yield of soft x-ray absorption in oxides is of the order of 50 Å.

Soft X-ray Source

All experiments in this dissertation were performed at Dragon beamline (BL-11A) in National Synchrotron Radiation Research Center (NSRRC),

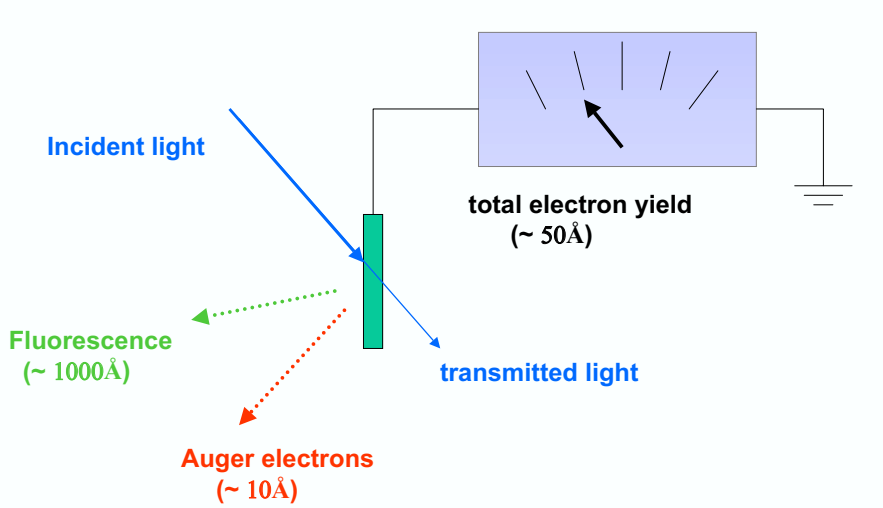

Figure 2.9: Illustration of the detection methods for soft x-ray absorption. Four different methods for measure the absorption spectra. An electro-meter is used for the total electron yield mode.

Taiwan. The 1.5 GeV electron storage ring in NSRRC is a circumference of 120 meters. Synchrotron radiation is produced from a bending magnets.

Figure 2.10 sketches the lay-out of the Dragon Beamline [16]. The monochromators of the Dragon beamline is a spherical grating monochromators [16]. The soft x-ray range can be covered by using the grating monochromators in grazing incidence. The ruling density of grating monochromators is 1200 lines per millimeters (1200 l/mm, $2d \sim 6 \times 10^{-7}$ meter) with energy region in between 400 eV and 1200 eV for XAS of transition-metal oxides. The entrance slit improves the resolution by making the monochromater less dependent on the light-source size, and exit slit moves during the energy-scan. The energy resolution is ~100 meV when the opening of entrance and exit slits are 20 μm and 20 μm, respectively. The resolving power ($\frac{E}{\Delta E}$) of dragon monochromators is 10000 with slit openings ~10μm. The end-station of

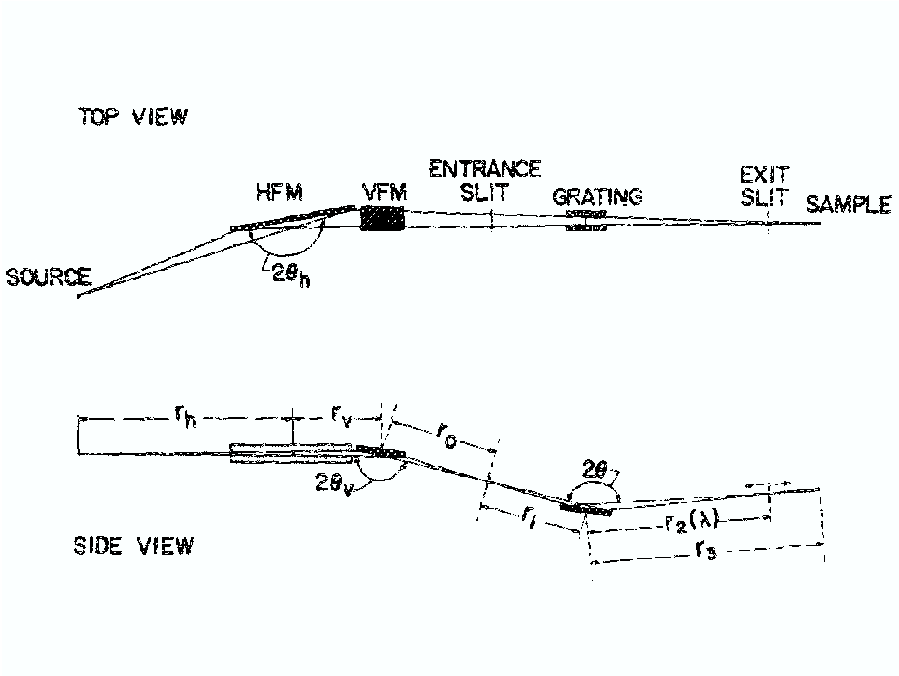

Figure 2.10: Schematic drawing of the Dragon beamline and monochromator. (from Ref. [16])

Dragon beamline is primarily designed for studying electronic structures of transition-metal oxides.

XAS Measurement System

The XAS chamber design is for investigating the electronic structure in the transition metal oxide, especially the LD in XAS which determining the orbital physics. A schematic representation is shown in Figure 2.11. The main-chamber is equipped with a XYZ manipulator used for the precise control of the sample position. A three-way-cross chamber is fixed at the bottom of the chamber which is connected to a vacuum pump system and pressure gauges. This chamber is equipped with an Alcatel Drytel-31 me-

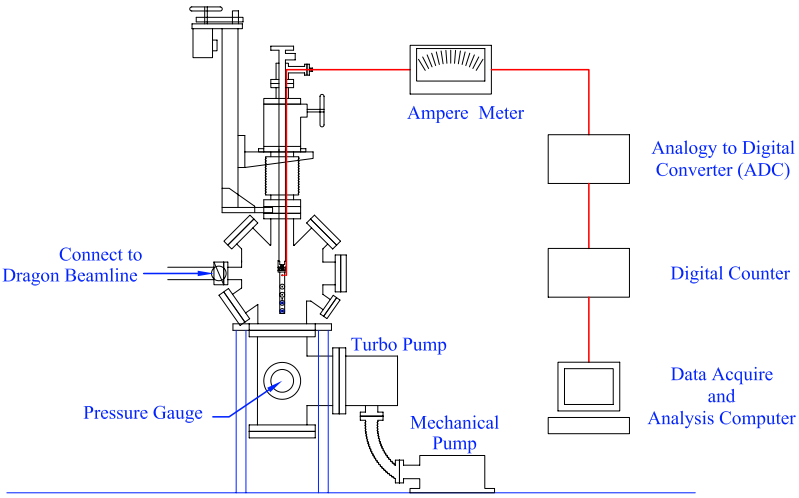

Figure 2.11: Schematic drawing of the apparatus utilize for the measurement during XAS experiments.

chanical pump and a Seiko-Sekei STP-300 turbo pump. The base pressure of this chamber can reach to near 3×10^{-9} torr without bake-out. After baking the system at $120 \sim 150°$ C for $6 \sim 9$ hours, the pressure of the chamber can be lower than 2×10^{-10} torr. At the opposite side of the entrance port of synchrotron radiation, a 4.5-inches window with a phosphor screen is used to aline the chamber position. Generally, we collect the sample drain current to obtain the XAS spectra. If the sample is an insulator, we either evaporated copper strips on samples or used a channeltron for the fluorescence yield to resolve the charging problem. However, this chamber can put a channeltron detector for collect the fluorescence yield XAS spectra from insulator samples.

Because the transition temperature of metal oxides are extraordinary wide, we designed a new cryo-stage which can cool down and warm up the sample temperature from 80 K to 450 K. The sample holder is fixed on the cold-finger of the cryo-stage. To measure the drain current, the sample holder is isolated from the cold finger with a Kypton sheet or sapphire plate between the sample holder and cold finger. As show in Fig. 2.11, an electric wire (in red) is connected between the sample holder and an electric feedthrough (BNC-type) to collect the drain current. An analog signal is measured by a current meter and then converted to a digital signal for data acquisition.

Rotary Sample Holder

Figure 2.12 represents the details of the specially designed sample holder for linear dichroism measurements. Four rotary sample holders and three fluorescent posts are mounted on one side of the base holder. One the other side, there is a groove for inserting a screwdriver with which we can be able to rotate the sample in vacuum. Figure 2.12(A) displays the picture of this rotary sample holder.

A pair of thermocouple is mounted on one sample holder to precisely monitor the sample temperature. A small spring is inserted between the base holder and rotary disk to improve thermo-conductivity; vacuum grease is spread between them for smoothly rotation. When this holder is fixed on the cryo-stage, the temperature of samples can be cooled down to 80 K with liquid nitrogen.

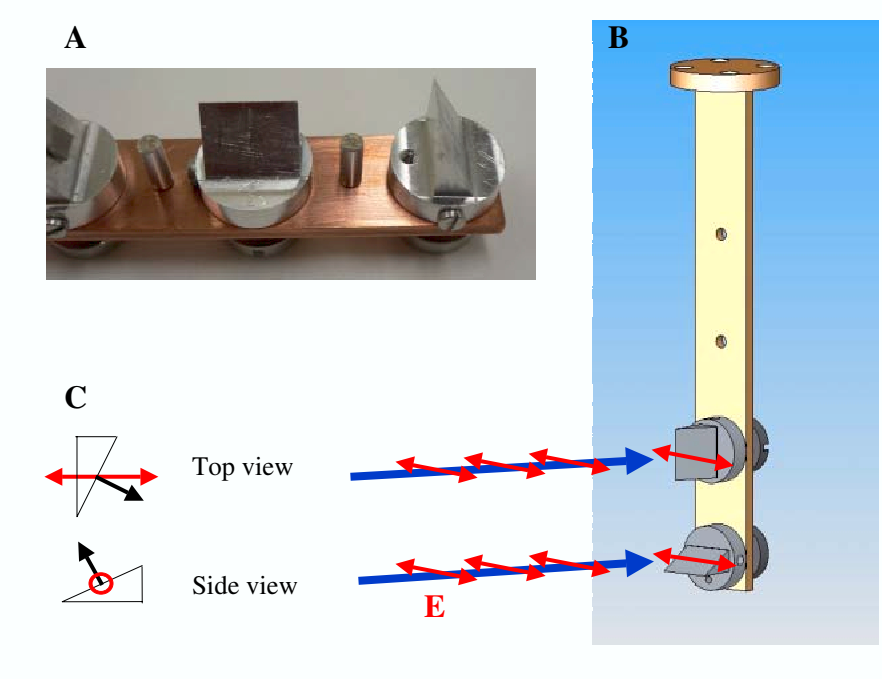

Figure 2.12: The rotary sample holder shown in different views, (A) and (B). (A) The sample holder photo. Red arrows in (B) show the **E** vector of the incident photons. (C) Orientations of the sample corresponding to the **E** vector perpendicular to c-axis and with an angle of 30° from the sample surface normal.

For linear dichroism experiments, the incident angel was always 60^o from the sample surface normal. We use a screwdriver to rotate the sample about the direction of incident photons to obtain the polarization dependent spectra. Figure 2.12 (B) and (C) show the schematic diagram of LD experimental technique. When the c-axis of sample is perpendicular to the **E** vector of incident photons, we denote the absorption intensity as $I_\perp$ for $\mathbf{E} \perp c$, as shown in the lower panel of Fig. 2.12(C). The absorption intensity in the upper panel of Fig. 2.12(C) is marked as I. With the geometry of the absorption taken into account, one can write the absorption intensity $I_\parallel$ for $\mathbf{E} \parallel c$ as

follows,

$$I_{\parallel} = \frac{4}{3}(I - \frac{4}{1}I_{\perp}). \tag{2.8}$$

All measured polarization-dependent XAS spectra referred to the **E** vector parallel to c axis are thus corrected the geometry effect. The difference in optical path and probing area could be eliminated.

2.3 Epitaxial Thin Films Growth in Pulsed Laser Deposition

Since the discovery of high-T_c superconductors, a great deal of attention has been focused to the development of the epitaxy techniques of transition-metal oxides. Now, more and more sophisticated methods have been demonstrated to successfully fabricate smooth and stoichiometric oxide films for device applications. The complex compositions of oxide thin films such as high-T_c superconductors or colossal magnetoresistance materials are not easy to fabricate by the conventional technique of molecular beam epitaxy (MBE). Pulsed-laser deposition (PLD) is one important technique for synthesize complex metal oxides thin films.

2.3.1 Advantage of Pulsed Laser Deposition

In contrast to semiconductors and metals, oxide films have to be grown with a high oxygen pressure. In order to achieve the desired oxygen stoichiometry in these thin films, it's necessary to use a wide range of oxygen pressure from ultrahigh vacuum to atmospheric pressure, and the substrate temperatures ranging from room temperature to well over 1000° C are necessary for thin film growth. Oxide thin film growth and their electrical properties are sensitive to these two parameters. For fabrication of high-quality oxide films, a deposition system equipped with a sample holder which delivers a wide ranges of sample temperature is necessary. In order to study the growth mechanism of oxide thin film, the deposition system compatible with

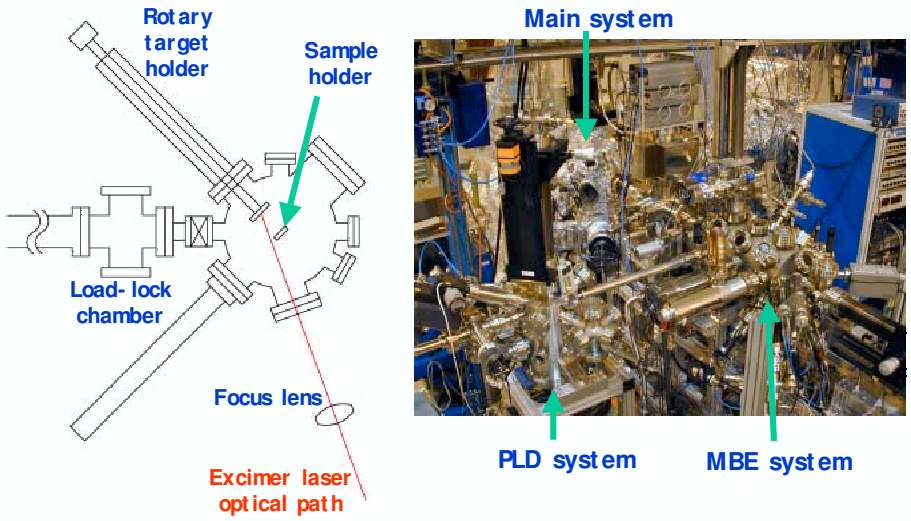

Figure 2.13: **Left**: Schematic diagram of the PLD chamber. **Right**: Photograph of the PLD system combined with the MBE system and the spectroscopy system. The samples, which grown in PLD system, can be easily transferred into the spectroscopy chamber for spectroscopy measurements with synchrotron radiation.

reflection high energy electron diffraction (RHEED) is important.

2.3.2 Pulsed Laser Deposition System Setup

Our PLD chamber is shown in Figure 2.13. A pulsed KrF excimer laser beam is introduced into the chamber at an angle of 25° from the surface normal of targets. The excimer laser beam is focused by a single lens before entering the chamber through a fused silica quartz viewport. Focusing optics with a nominal working distance of 500 mm provides a spot size of 3 mm × 1 mm on the target. A carousel target holder to have a capacity of six targets and could be rotated during deposition. In this way, most of the target surface is therefore used for ablation and excessive damage to the target surface is prevented. High-purity oxygen (99.995 %) gas is supplied into the chamber. Gas flow is regulated with a manual variable leak valve.

An *in-situ* reflection high energy electron diffraction (RHEED) monitoring employ for fabricating high quality thin films.

A. Laser

Generally, the wavelengths of laser for thin-film growth in PLD are between 200 nm to 400 nm. In this spectral region, most materials exhibit strong absorption during the deposition. When one moves to the short-wavelength end of this range, absorption coefficients tend to increase but the penetration depths in the target materials are correspondingly reduced. This is a favorable situation when the wavelength is close to 200 nm, because thin layers of the target surface are ablated. In addition, the strong absorption in short wavelength results in a decrease in ablation fluency thresholds; the optics are also more difficult.

Within a range between 200 nm to 400 nm, there are only few commercially available laser sources capable to deliver high-energy densities (>1 J/cm^2) in large areas (10 mm^2 or larger) for laser deposition. Most of the work accomplished to date have centered around excimer and Nd^{3+}:YAG lasers as the deposition source.

Nd^{3+}:YAG laser is a solid-state system. The neodymium ions are active medium and as impurities in the YAG (yttrium aluminum garnet) host. The output energies are up to 2 J/pulse. However, the fundamental laser emission of Nd^{3+}:YAG is at 1064 nm, which is out of the desired range of wavelength. Using a nonlinear crystal or mixing with the residual 1064 nm light after

Table 2.2: Operating Wavelengths of Excimer Laser.

Excimer	Wavelength (nm)
F_2	157
ArF	193
KrCl	222
KrF	248
XeCl	308
XeF	351

one frequency doubler, the resulting outputs at 266 nm and 355 nm are produced with efficiencies of ∼15 % and ∼20 % relative to the fundamental frequency, respectively. This is a complex process to achieve the desired range of wavelength.

Excimer is a gas laser system. Unlike Nd^{3+}:YAG lasers, the wavelength of excimer lasers are directly in the UV range, and high-power outputs are commercially available. Table 2.2 shows the active excimer molecule and the corresponding wavelengths of commercial laser systems. KrF is the most popular choice among the PLD community, because of the highest gain system for electrically discharged pumped excimer lasers. Although the wavelength of KrCl excimer is shorter than KrF, however, it's a low-gain system and output pulse energies are not enough for PLD required. Here, we chose the KrF excimer laser for our PLD system.

B. Optical Elements

In a system of pulsed laser deposition, one of the most important parameter is the power density of laser, which determines the film stoichiometry

Table 2.3: Transmittance Range of Various Materials.

Material	Transmittance Range (nm)
Magnesium fluoride	140∼7500
Sapphire	150∼5000
Calcium fluoride	150∼8000
UV-grade fused silica	190∼2500
Borosilicate crown glass	315∼2350

and the crystallographic quality. The optical elements collect the radiation from the laser source and focus the laser beam to a corresponding point on the target to achieve the required power density. Not only for the required power density but also for preventing the damage to the optical elements, keeping the optics clean is important.

Optical elements are placed between the output port of the laser and the view point of the deposition chamber in order to steer and to focus the laser beam. The optical elements in our PLD system are six mirrors, one aperture, one focus lens, and one laser windows (view-port). One needs to consider the materials of lens and the transmittance range for a PLD system. Table 2.3 lists some materials of commercial lenses with corresponding transmittance ranges. For a pulsed laser deposition system with a KrF excimer laser of 248 nm, we chose UV-grade fuced-silica lenses.

C. Chamber Design

The schematic drawing of the PLD system is shown in the Fig. 2.14 with top- and side-views. Our UHV chamber is with a diameter of 262 mm and a height of 380 mm. This chamber is equipped with two turbo pumps. One

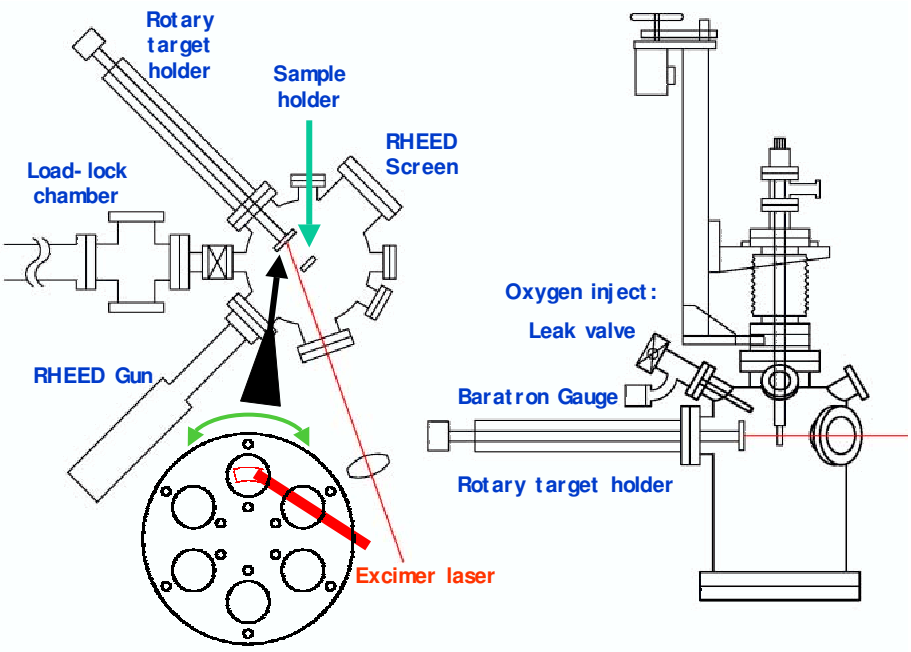

Figure 2.14: The schematic drawing of our PLD system. Left and right panel is the top- and side-view, respectively.

is a 400 l/s pump for pressure below 10^{-4} torr; the other is a 100 l/s turbo pump for sample transfer from a load-lock chamber to the PLD chamber. An oil-free mechanical pump is used for roughing the turbo pump. The base pressure is lower than 1×10^{-8} torr. The pressure of the chamber is monitored with a conventron gauge, a Baratron gauge, and an ion gauge.

High-purity oxygen gas is supplied into PLD chamber through a nozzle pointing toward the substrate with a distance of 5 cm to locally increase the oxygen concentration around the sample. As shown in the right panel of Fig. 2.14, the flow of gas is regulated with a variable leak valve. The Baratron gauge monitors the pressure before oxygen molecules pass through the nozzle.

The use of RHEED in an oxygen environment is limited by the oxidation of the tungsten filament in the electron gun. Therefore, the PLD chamber is equipped with a differentially pumped RHEED gun for *in-situ* monitoring surface structure. With this combination of oxygen nozzle inlet and differentially pumped RHEED, the film surface can be monitored by the intensity oscillation of RHEED specular reflection even in highly oxidizing conditions.

The carousel target holder which can accommodate 6 targets is shown in lower-left panel of Fig. 2.14. The ablation targets are mounted on target holders. The carousel is mounted on a translational-stage combined with a rotary feedthrough driven by a stepping motor for carousel rotation. During the growth, the carousel rotates back and forth with an angle of 20° at a speed of $\frac{1}{6}$ r.p.m. Such a mechanism makes the unmovable laser beam to sweep a curve on the target and prevents excessive damage to the target.

The sample holder is equipped an button heater, which can be operated at 1000° C in an atmosphere pressure for a life-time longer than 1000 hours. The holder is made with inconel, a special material which resists oxidation under a high-pressure oxygen enviroment at high temperature. A type-K thermocouple is mounted on the holder to monitor the temperature during the deposition, and an optical pyrometer calibrated with the thermocouple, is used for measuring the substrate temperature. The substrate temperature can reach to 650° C when the holder is equipped with thermo-shielding. A substrate crystal is attached to the holder with stainless-steel clamps.

In the RHEED experiment, a primary electron beam with a kinetic en-

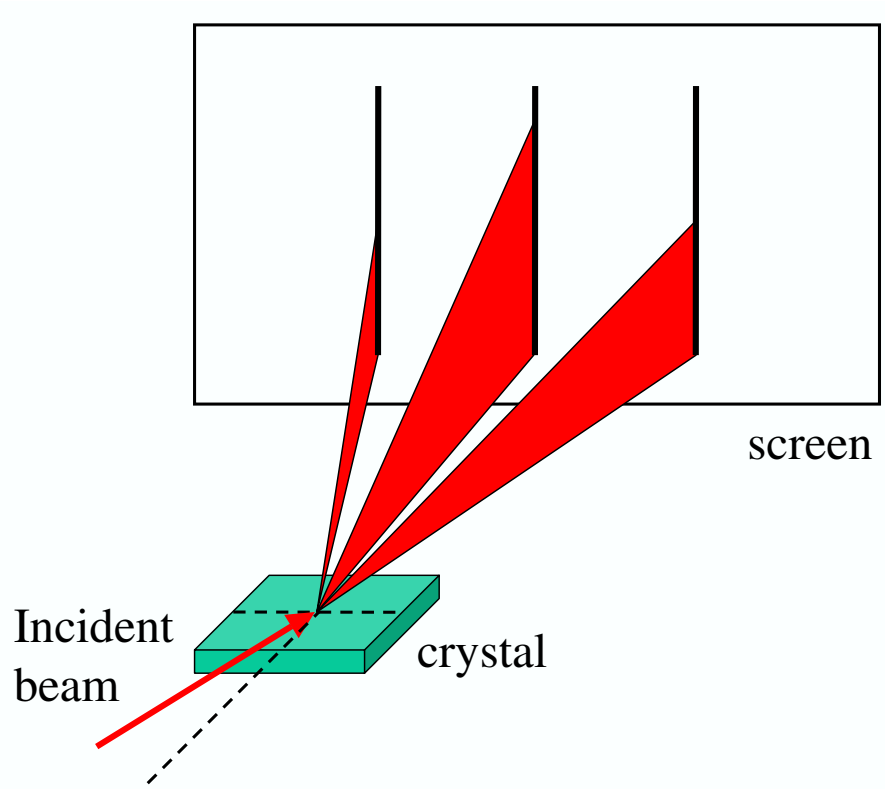

Figure 2.15: A schematic drawing of the experimental geometry of RHEED experiment.

ergy of 10∼30 KeV impinges on a crystal surface at grazing incidence (0.5° ∼ 3°). After reflection, the diffraction patterns are observed with a fluorescent screen. The intensity of the RHEED specular beam is monitored with a 8-bit high-resolution digital CCD video camera and digitized with a computer for real-time analysis during the deposition. Figure 2.15 shows schematic drawing of the experimental geometry of RHEED experiment. The diffraction conditions occurs when the reciprocal lattice rods intersect with the Ewald sphere.

In addition, the RHEED specular spot intensity plotted as a function of time is used to determine the growth rates and the layer thicknesses, and the

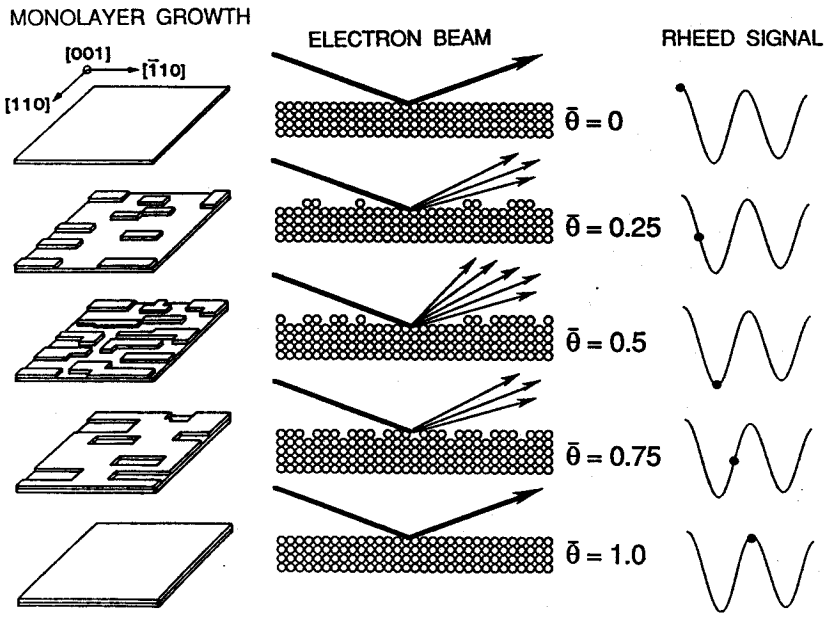

Figure 2.16: Real space representation of the formation of a single complete monolayer; $\overline{\theta}$ is the fractional layer coverage; corresponding RHEED oscillation signal is shown. (from Ref. [19])

oscillation of intensity is called as RHEED oscillation. The process involved in layer-by-layer growth can be described by a model introduced by Cohen *et.al.* [18]. As shown in Fig. 2.16, the *breath-death* model describes the growth process in terms of the $0 \leq \bar{\theta} \leq 1$. New step edges appear when new islands nucleate; the diffuse scattering is at the expense of specular spot intensity causing the RHEED intensity to drop ($\bar{\theta} = 0.5$). As the deposition continues, islands coalesce and the specular spot intensity increases again until forming a complete monolayer ($\bar{\theta} = 1$). RHEED intensity oscillations reflect the periodic change in the surface morphology associated with two-dimensional layer-by-layer growth.

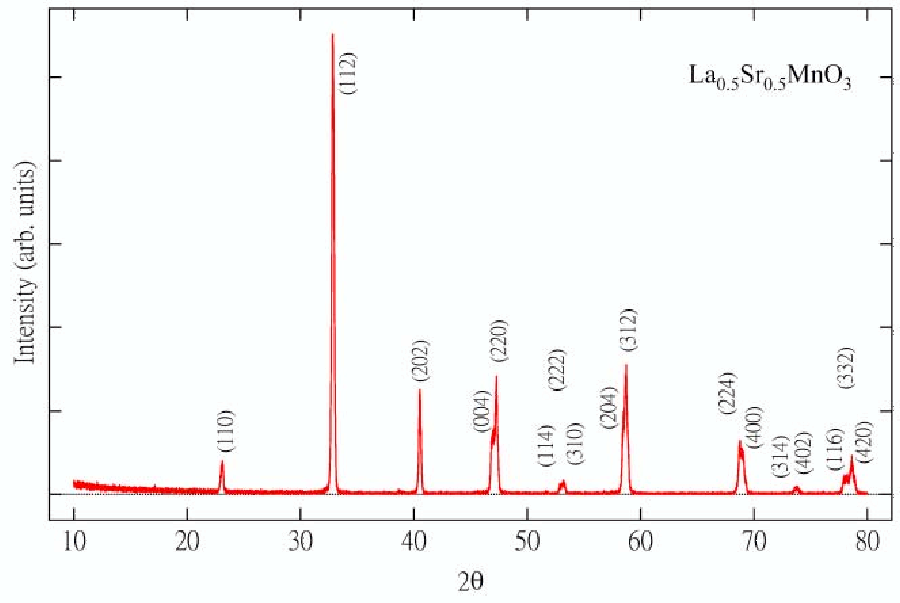

Figure 2.17: θ-2θ powder XRD of $La_{0.5}Sr_{0.5}MnO_3$ polycrystalline targets measured with a Cu K_α x-ray source of $\lambda = 1.5405$ Å.

2.3.3 Epitaxial Growth of $La_{0.5}Sr_{0.5}MnO_3$ Thin Films

A. Target Preparation

Polycrystalline samples of $La_{0.5}Sr_{0.5}MnO_3$ were prepared by the solid-state reaction method. The appropriate molar quantities of La_2O_3, $SrCO_3$, and Mn_2O_3 powders were ground and pre-fired in air at 1000° C for 24 hours. The calcined powder was then ground again, well mixed and pressed into pellets. These pellets were sintered at 1100° C for 48 hours in air and cooled down to room temperature with a rate of 5° C/min. These pellets were ground again. The process was repeated until the confirmation of single phase in perovskite structure with powder x-ray diffraction (XRD) measurements using Cu K_α x-ray source. A typical θ-2θ XRD pattern is shown in Fig. 2.17.

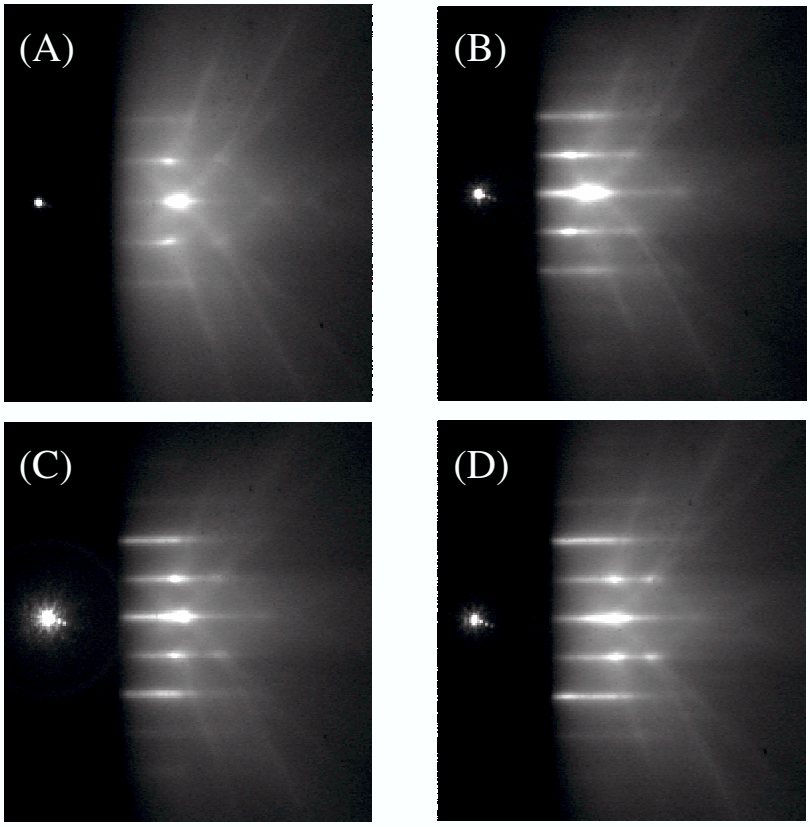

Figure 2.18: (A)&(B): RHEED patterns of $SrTiO_3$(001) substrate before and after annealing in an oxygen atmosphere. (C)&(D): RHEED patterns of $La_{0.5}Sr_{0.5}MnO_3$ films grown on $SrTiO_3$(001) before and after post-annealing.

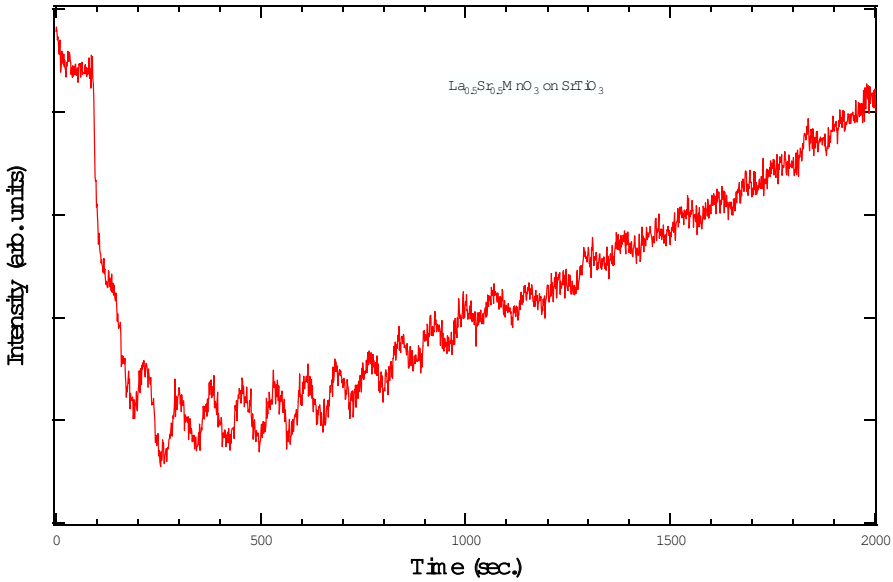

Figure 2.19: Time dependence of the RHEED specular beam intensity during the growth of $La_{0.5}Sr_{0.5}MnO_3$ films on $SrTiO_3$(001).

B. Growth Process

Thin films of $La_{0.5}Sr_{0.5}MnO_3$ have been fabricated on single crystalline perovskite substrates, $SrTiO_3$ (lattice constant of 3.905 Å). The substrates were cleaned with acetone and dried with nitrogen. Prior to the deposition, the substrates were in-situ annealed for 30 min at the temperature about 630° C and 1×10^{-4} torr of oxygen atmosphere. Thin films were deposited at 1×10^{-4} torr of oxygen pressure by impinging KrF excimer laser pulses of 150 mJ on a target. The pulse rate of the KrF laser was 1 Hz. The laser power density at the target surface was 4 J/cm^2. The distance between target and substrate was 30 mm. The deposition of the films were at a rate of 0.33 Å/sec with the substrate temperature maintained at 630° C. After the deposition, the films were annealed in the 5×10^{-3} torr oxygen at 630° C for 100 min, and then cooled slowly to room temperature at a rate of 7° C/min.

Polished and acetone cleaned $SrTiO_3$ substrates were used. Figure 2.18(A) shows the RHEED pattern of $SrTiO_3$ without any treatment. The bright spot, so called the "straits through" spot, results from the incident electron beam which is not blocked by the sample surface. After *in-situ* annealing in an oxygen atmosphere (10^{-4} torr) at 630° C, Fig. 2.18(B) shows that the RHEED pattern of stripes with equal spacing. The central three diffraction rods and the parabolic Kikuchi lines were clearly appear, indicating of good crystalline order. After deposition, the RHEED pattern of $La_{0.5}Sr_{0.5}MnO_3$

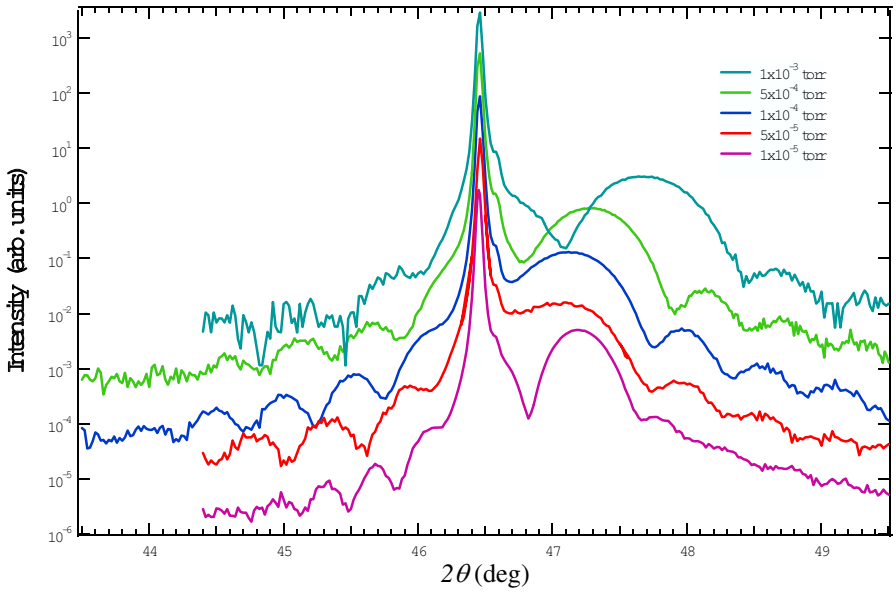

Figure 2.20: X-ray diffraction of epitaxial $La_{0.5}Sr_{0.5}MnO_3$ films on $SrTiO_3(001)$ with a Cu K_α x-ray source of $\lambda = 1.5405$ Å.

on $SrTiO_3(001)$ thin film grown on $SrTiO_3(001)$ is shown in Fig. 2.18(C). With further post-annealing, Fig. 2.18(D) shows that the diffraction rods and parabolic Kikuchi lines of RHEED pattern were much sharper than in Fig. 2.18(C), revealing good crystalline order.

Figure 2.19 shows the RHEED oscillations observed during the deposition of $La_{0.5}Sr_{0.5}MnO_3$ on $SrTiO_3(001)$. Each oscillation corresponds to the formation of one atomic monolayer (ML), indicating a 2-dimensional layer-by-layer growth.

C. X-ray Diffraction

A θ-2θ x-ray diffraction pattern of the $La_{0.5}Sr_{0.5}MnO_3$ films on various oxygen pressure conditions are shown in Fig. 2.20. The pronounced interfer-

ence fringes were observed in every thin film samples as shown in Fig. 2.20, showing evidence of small roughness at the interface.

The lattice constant of the bulk $La_{0.5}Sr_{0.5}MnO_3$ is 3.86 Å, and that of $SrTiO_3$ is 3.905 Å.

In the x-ray diffraction studies, the Bragg peaks of thin films fabricated in different oxygen pressure, suggest that 1×10^{-4} torr of oxygen pressure is the best condition to grow $La_{0.5}Sr_{0.5}MnO_3$ films on a $SrTiO_3$ substrate in our PLD system.

Reference

[1] F. M. F. de Groot, Coordination Chemistry Reviews **249**, 31-36 (2005).

[2] P. Hohenberg and W. Kohn, Physical Review **136**, B864 (1964).

[3] W. Kohn and L. J. Sham, Physical Review **140**, A1133 (1965).

[4] F. M. F. de Groot, J. Faber, J. J. M. Michiels, M. T. Czyżyk, M. Abbate, and J. C. Fuggle, Phys. Rev. B **48**, 2074 (1993).

[5] P. H. Butler, Point Group Symmetry Applications: Methods and Tables, Plenum Press, New York (1981).

[6] A. Fontaine, Interaction of X-ray With Matter: Absorption Spectroscopy, HERCULES, Grenoble Vol.1 (1995).

[7] S. Sugano, Y. Tanabe and H. Kamimura, Multiplets of Transition Metal Ions, Academic Press, New York (1970).

[8] F. M. F. de Groot, J. C. Fuggle, B. T. Thole and G. A. Sawatxky, Phys. Rev. B **41**, 928 (1990).

[9] F. M. F. de Groot, J. Electron Spectrosc. Relat. Phenom **67**, 5294 (1994).

[10] J. C. Slater, Phys. Rev. **34**, 1293 (1929).

[11] E. U. Condon, Phys. Rev. **36**, 1121 (1930).

[12] E. U. Condon and G. H. Shortley, Phys. Rev. **37**, 1025 (1931).

[13] J. C. Slater, Theory of Atomic Structure, McGraw-Hill, (1960).

[14] C. T. Chen *et al.*, Phys. Rev. Lett. **66**, 104 (1991).

[15] M. Abbate, J. C. Fuggle, A. Fujimori, L. H. Tjeng, C. T. Chen, R. Potze, G. A. Sawatzky, H. Eisaki and S. Uchida, , Phys. Rev. B **47**, 16124 (1993).

[16] C. T. Chen and F. Sette, Rev. Sci. Instr. **60**, 1616 (1989).

[17] I. Hernandez-Calderon and H. Hochst, Phys. Rev. B **27**, 4961 (1983).

[18] P. I. Cohen, G. S. Petrich, P. R. Pukite, G. J. Whaley, and A. S. Arrot, Surf. Sci. **216**, 222 (1989).

[19] Milton Ohring. *The Materials Science of Thin Films.* Academic Press, INC., 1250 Sixth Avenue, San Diego, CA 92101, (1992).